Post-Annealing Effects on the Structural and Optical Properties of Zn(S,O) Buffer Layer for Thin-Film Solar Cells

후열처리에 따른 Zn(S,O) Buffer Layer의 구조적, 광학적 특성 변화

2013년 2월

서울대학교 대학원

재료공학부

이 성 준

Post-Annealing Effects on the Structural and Optical Properties of Zn(S,O) Buffer Layer for Thin-Film Solar Cells

후열처리에 따른 Zn(S,O) Buffer Layer의 구조적, 광학적 특성 변화

지도교수 박 병 우

이 논문을 공학석사 학위논문으로 제출함.
2013년 2월

서울대학교 대학원
재료공학부
이 성 준

이성준의 공학석사 학위논문을 인준함.

2013년 2월

위 원 장   유 상 임

부위원장   박 병 우

위 원   박 찬

Abstract

The structural and optical properties of Zn(S,O) buffer layers were investigated by post-annealing in air. As the annealing temperature increased to 500°C, the optical bandgap of the Zn(S,O) thin films decreased from 3.59 eV to 2.97 eV. This optical bandgap narrowing was correlated with the composition change of the films by post-annealing. The S/Zn ratio decreased from 0.60 to 0.47, as confirmed by EDX analysis. The Zn(S,O) thin film applied to blocking layer in dye-sensitized solar cells diminished the power-conversion efficiency. One possible reason is that the Zn(S,O) blocking layer prohibits the injection of electron from ZnO to FTO, because of thick Zn(S,O) layer.

Micrometer-sized polydispersed Al doped ZnO aggregates made up of nanoparticles were synthesized by a hydrolysis method for photoelectrode in DSSCs. The Al doping on ZnO aggregates resulted the decrease of open-circuit voltage (V_{oc}) and short-circuit current (J_{sc}). Consequently, the power-conversion efficiency decreased to 0.92%. The local strain and grain size of ZnO increased with increasing doping concentration. In addition, the morphology of ZnO nanoparticles that compose the aggregates was changed to nanorod. The nanorod will decrease the surface area for dye adsorption than nanoparticle and it may cause decreased cell efficiency.

Table of Contents

List of Figures

Chapter 2.

List of Figures

deposited times.   The inset shows power-conversion efficiency of DSSCs as a function of the blocking layer deposition times.

List of Figures

Chapter 3.

List of Tables

Chapter 1. Overview

1.1. CIGS Solar Cells

1.1.1. General Introduction to CIGS Solar Cells

Over the last decades, the fossil fuels of the earth are rapidly being depleted and the demand for highly efficient, low cost and non-polluting sources of energy is intensely increasing. In our need for renewable and eco-friendly energy, photovoltaics are considered as the most promising solution of the energy supply problem.

The $Cu(In,Ga)Se_2$ (CIGS) thin-film solar cells have attracted for use in photovoltaic devices, owing to their relatively high efficiency in both large area and laboratory-sized solar cells [1,2]. The highest efficiency of CIGS solar cells is 19.9% in laboratory scale [3]. As compared with wafer based Si solar cells, thin-film solar cells can be easily deposited on large areas of glass [4,5], steel [6], or even polyimide substrates, which would make these solar cells lightweight [7].

1.1.2. Structure of CIGS Solar Cells

Figure 1-1 is a schematic diagram of the CIGS solar cells. Typically, soda lime glass is used as a substrate but other substrates can be used for desired properties of the device. The Na content of the glass plays an important role during the deposition of the CIGS absorber. The Na has positive effects on both electronic and structural properties of CIGS and increases the efficiency of final devices [8]. Molybdenum back contact is deposited by evaporation or sputtering. On top of the back contact, the CIGS absorber layer with 2-3 μm thickness is deposited. The bandgap of $Cu(In_xGa_{1-x})Se_2$ can be changed by altering the Ga/(In+Ga) ratio. The bandgap range of Cu-chalcopyrite materials is from 1.04 eV ($CuInSe_2$) to 1.68 eV ($CuGaSe_2$) [9]. The buffer layer is deposited by chemical bath method (CBD) for improving the device performance. The ZnO window layer is deposited on the buffer layer. This window layer consists of an intrinsic ZnO layer and Al doped ZnO layer. The intrinsic ZnO layer prevents Al diffusion from Al doped ZnO layer to buffer layer [10].
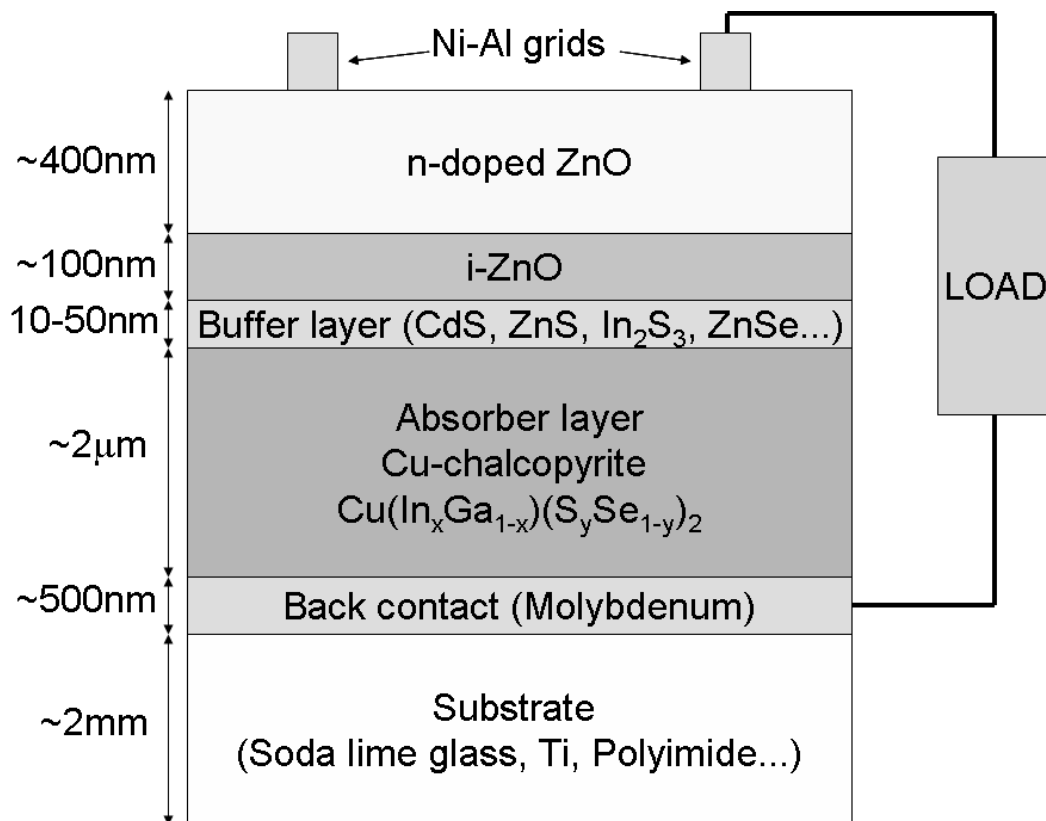
Fig. 1-1. Schematic diagram of the layer sequence in a CIGS solar cell [11].

1.2. Buffer Layer of CIGS Solar Cells

1.2.1. The Role of Buffer Layer

The primary function of the CdS buffer layer in the CIGS solar cells is protecting the CIGS layer from the sputtering damage during the deposition of a subsequent transparent conducting oxide (TCO) layer [12].   It also reduces the recombination of the electron-hole pairs around the absorber-window, and this is achieved in two ways.   The buffer layer minimizes the lattice mismatch and makes spike conduction band offset, thus achieving an increased open circuit voltage [13-16].   The band diagram for a ZnO/CdS/CIGS solar cell is shown in Fig. 1-2.

1.2.2. Advantage of Zn(S,O) buffer layer

CdS is the most typically used material for high efficiency CIGS solar cells. However, CdS has an environmental problem due to the toxicity of cadmium.   Moreover, the low bandgap of CdS (2.4 eV) causes optical absorption loss at short wavelength region [17].   For these reasons, several materials, such as Zn(S,O), ZnSe, In_2S_3, and ZnMgO, have been investigated as an alternative to CdS buffer layer [12,18-20]. Among these alternative materials, chemical bath deposited Zn(S,O) (CBD-Zn(S,O)) is considered as the most promising buffer layer, because it is non-toxic and has a large bandgap (3.6 eV).   The external quantum efficiencies of $CuInS_2$ based device are shown in Fig. 1-3.   Due to the higher energy bandgap of Zn(S,O), a net current gain of 1 mA/cm^2 is achieved by replacing the CdS [21,22].
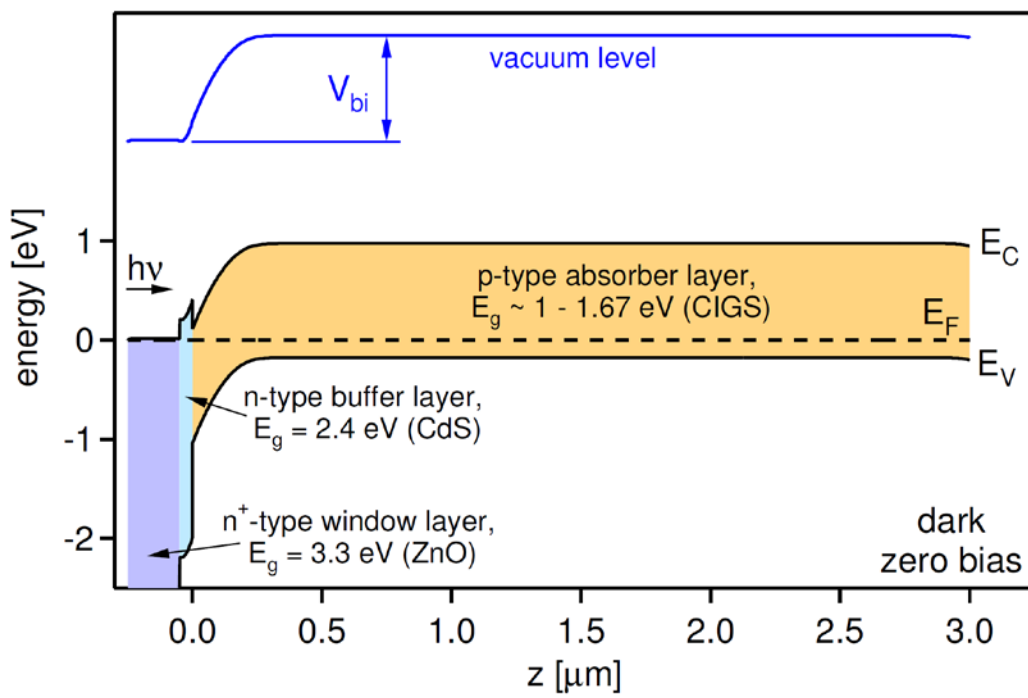
Fig. 1-2.   Energy band diagram of a CIGS/CdS/ZnO thin films [23].
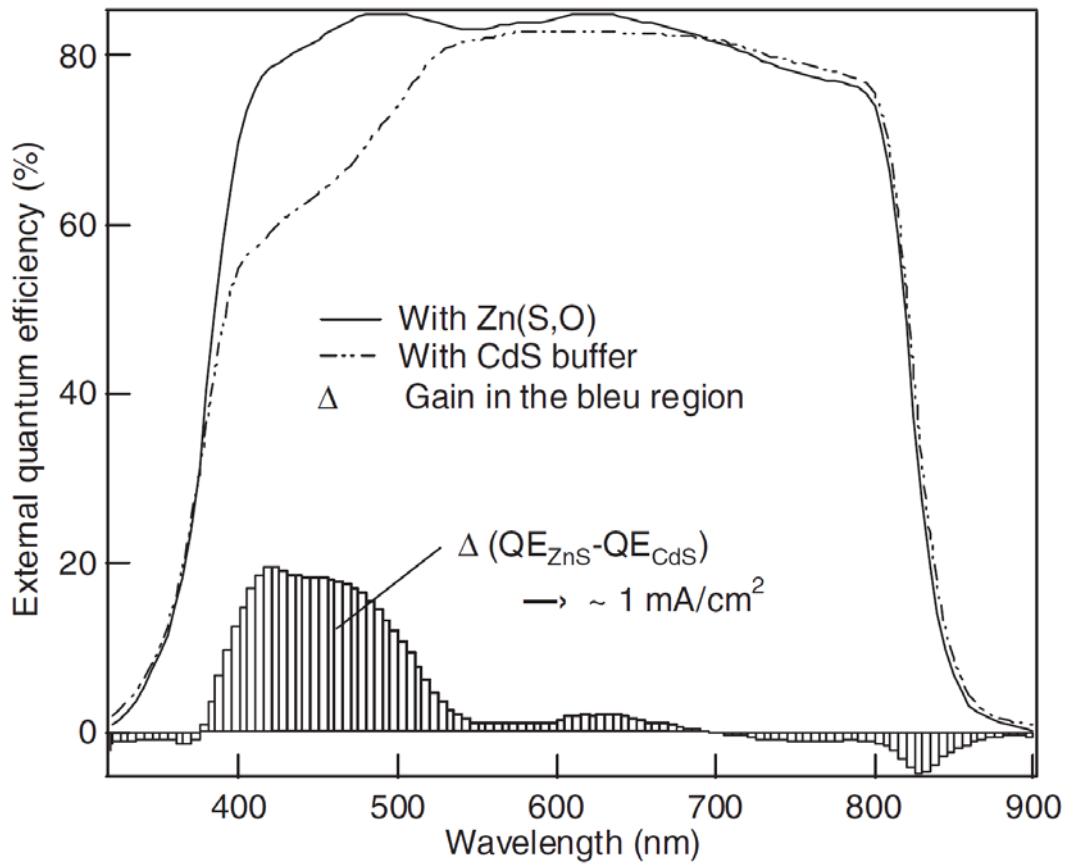
Fig. 1-3. The external quantum efficiencies of $CdS/CuInS_2$ and $Zn(S,O)/CuInS_2$ based device. The difference of the external quantum efficiencies between $Zn(S,O)$ and CdS buffer layer is 1 mA/cm^2 [22].

1.3. Dye-Sensitized Solar Cells

1.3.1. General Introduction to Dye-Sensitized Solar Cells

Dye-sensitized solar cells (DSSCs) are one of the potential candidates for next-generation solar cells due to their high durability, large flexibility in shape, color, low cost and transparency [24-26]. In 1991, Grätzel and O'Regan reported the dye-sensitized nanocrystalline TiO_2 solar cell structure [27]. Since then, the power conversion efficiency of the DSSCs have been developed rapidly and the DSSCs achieve maximum efficiency of 12.3% and lifetime of 10,000 h [26,28].

The DSSCs are a photoelectrochemical system, which consist of four primary parts (Fig. 1-4). A mesoporous oxide film composed of a network of TiO_2 nanoparticles which serves as the photosensitized anode is deposited on transparent conducting oxide (TCO) substrate, and the platinum coated fluorine-doped tin oxide (FTO) glass acts as the counter electrode [25,29]. The liquid electrolyte, dissolved I^-/I_3^- redox couples play a role of a conductor to connect the two electrodes electrically [30]. Dye molecules attached on the surface of the TiO_2 nanoparticles absorb photons and generate excitons which are divided into electron and hole rapidly at the nanoparticle surface [31]. The injected electrons into the conduction band of the oxide can pass through the nanoparticles and flow into the external circuit. The redox mediator molecules regenerate the oxidized sensitizer dyes [32].
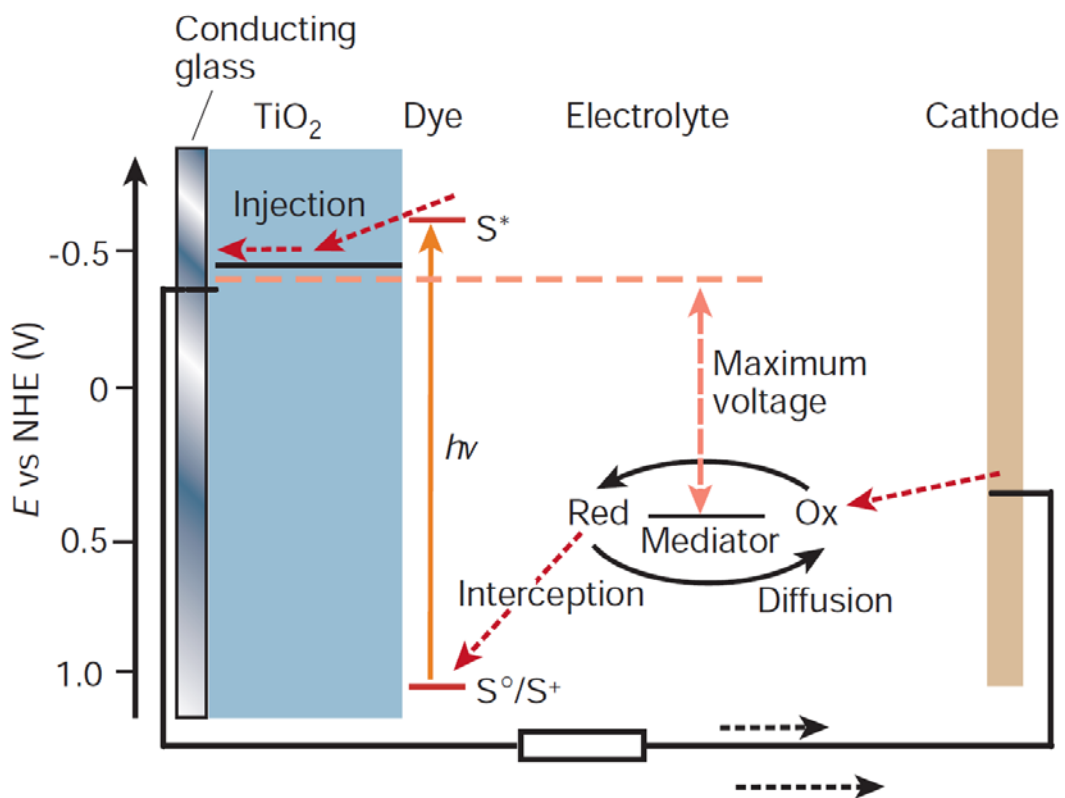
Fig. 1-4.   Principle of the dye-sensitized solar cell [30].

1.3.2. Advantages of ZnO-Based Dye-Sensitized Solar Cells

The photoelectrode is one of the important components in DSSCs. It should have large surface area for adsorbing sufficient dye molecules and make appropriate energy level alignment with dye. For the efficient electron injection from the dye molecules to the photoelectrode, the position of the conduction-band edge of photoelectrode should be lower than LUMO energy level of the dye [33]. TiO_2 is the commonly used oxide semiconductor for photoelectrode material, but ZnO is an attractive material for nanoscale optoelectronic devices, because it is a wide bandgap semiconductor with good carrier mobility. The conduction band of ZnO (-0.2V versus NHE at pH = 1) is similar to TiO_2 (-0.28V versus NHE at pH = 2) [34]. The carrier mobility of single-crystal ZnO is 115 - 155 cm^2/Vs, which is 2 orders of magnitude higher than 1 - 4 cm^2/Vs in TiO_2 [35,36]. Furthermore, different nanostructures such as spherical particles, rods, sheets, and tips can be obtained by various fabrication methods like sol-gel synthesis, chemical bath deposition, hydrothermal/solvothermal growth, and electrochemical deposition [37].

1.4. References

1. C. H. Liu, C. H. Chen, S. Y. Chen, Y. T. Yen, W. C. Kuo, Y. K. Liao, J. Y. Juang, H. C. Kuo, C. H. Lai, L. J. Chen, and Y. L. Chueh, "Large scale single-crystal Cu(In,Ga)Se$_2$ nanotip arrays for high efficiency solar cell," *Nano Lett.* **11,** 4443 (2011).

2. S. Wang, G. Xia, J. Shao, and Z. Fan, "Structure and UV emission of nanocrystal ZnO films by thermal oxidation of ZnS films," *J. Alloys Compd.* **424,** 304 (2006).

3. I. Repins, M. A. Contreras, B. Egaas, C. DeHart, J. Scharf, C. L. Perkins, B. To, and R. Noufi, "19.9%-efficient ZnO/CdS/CuInGaSe^2 solar cell with 81.2% fill factor," *Prog. Photovolt: Res. Appl.* **16,** 235 (2008).

4. D. Schmid, M. Ruckh, F. Grunwald, and H. W. Schock, "Chalcopyrite/defect chalcopyrite heterojunctions on the basis of CuInSe$_2$," *J. Appl. Phys.* **73,** 2902 (1993).

5. P. Jackson, R. Würz, U. Rau, J. Mattheis, M. Kurth, T. Schlötzer, G. Bilger, and J. H. Werner, "High quality baseline for high efficiency, Cu(In1-x,Ga x)Se$_2$ solar cells," *Prog. Photovolt: Res. Appl.* **15,** 507 (2007).

6. T. Yagioka, and T. Nakada, "Cd-free flexible Cu(In,Ga)Se$_2$ thin film solar cells with ZnS(O,OH) buffer layers on Ti foils," *Appl. Phys. Express* **2,** 072201 (2009).

7. R. Birkmire, E. Eser, S. Fields, and W. Shafarman, "Cu(InGa)Se$_2$ solar cells on a flexible polymer web," *Prog. Photovolt: Res. Appl.* **13,** 141 (2005).

8. P. T. Erslev, J. W. Lee, W. N. Shafarman, and J. D. Cohen, "The influence of Na on metastable defect kinetics in CIGS materials," *Thin Solid Films* **517,** 2277 (2009).

9. A. Shaukat, "Composition-dependent band gap variation of mixed chalcopyrites," *J.*

Phys. Chem. Solids **51,** 1413 (1990).

10. U. Rau, and M. Schmidt, "Electronic properties of ZnO/CdS/Cu(In,Ga)Se$_2$ solar cells - Aspects of heterojunction formation," *Thin Solid Films* **387,** 141 (2001).

11. R. S. Araoz, "Chemical bath deposition of Zn(S,O) buffer layers and application in Cd-free chalcopyrite-based thin-film solar cells and modules," *Dissertation*, Freien Universität Berlin (2009).

12. N. Naghavi, D. Abou-Ras, N. Allsop, N. Barreau, S. Bücheler, A. Ennaoui, C. H. Fischer, C. Guillen, D. Hariskos, J. Herrero, R. Klenk, K. Kushiya, D. Lincot, R. Menner, T. Nakada, C. Platzer-Björkman, S. Spiering, A. N. Tiwari, and T. Törndahl, "Buffer layers and transparent conducting oxides for chalcopyrite Cu(In,Ga)(S,Se)$_2$ based thin film photovoltaics: Present status and current developments," *Prog. Photovolt: Res. Appl.* **18,** 411 (2010).

13. S. W. Shin, S. R. Kang, J. H. Yun, A. V. Moholkar, J. H. Moon, J. Yong Lee, and J. H. Kim, "Effect of different annealing conditions on the properties of chemically deposited ZnS thin films on ITO coated glass substrates," *Sol. Energy Mater. Sol. Cells* **95,** 856 (2011).

14. A. Yamada, K. Matsubara, K. Sakurai, S. Ishizuka, H. Tampo, P. J. Fons, K. Iwata, and S. Niki, "Effect of band offset on the open circuit voltage of heterojunction CuIn$_{1-x}$Ga$_x$Se$_2$ solar cells," *Appl. Phys. Lett.* **85,** 5607 (2004).

15. A. Niemegeers, M. Burgelman, and A. Devos, "On The CdS/CuInSe$_2$ Conduction-Band Discontinuty," *Appl. Phys. Lett.* **67,** 843 (1995).

16. M. Bär, A. Ennaoui, J. Klaer, R. Sáez-Araoz, T. Kropp, L. Weinhardt, C. Heske, H. W.

Schock, C. H. Fischer, and M. C. Lux-Steiner, "The electronic structure of the [Zn(S,O)/ZnS]/CuInS$_2$ heterointerface - Impact of post-annealing," *Chem. Phys. Lett.* **433,** 71 (2006).

17. S. W. Shin, H. P. Oh, S. M. Pawar, J. H. Moon, and J. H. Kim, "Effect of complexing agent and annealing atmosphere on properties of nanocrystalline ZnS thin films," *J. Nanosci. Nanotechnol.* **10,** 3686 (2010).

18. C. Hubert, N. Naghavi, O. Roussel, A. Etcheberry, D. Hariskos, R. Menner, M. Powalla, O. Kerrec, and D. Lincot, "The Zn(S,O,OH)/ZnMgO buffer in thin film Cu(In,Ga)(S,Se)$_2$-based solar cells part I: Fast chemical bath deposition of Zn(S,O,OH) buffer layers for industrial application on Co-evaporated Cu(In,Ga)Se$_2$ and electrodeposited CuIn(S,Se)$_2$ solar cells," *Prog. Photovolt: Res. Appl.* **17,** 470 (2009).

19. A. Ennaoui, S. Siebentritt, M. C. Lux-Steiner, W. Riedl, and F. Karg, "High-efficiency Cd-free CIGSS thin-film solar cells with solution grown zinc compound buffer layers," *Sol. Energy Mater. Sol. Cells* **67,** 31 (2001).

20. D. Hariskos, S. Spiering, and M. Powalla, "Buffer layers in Cu(In,Ga)Se$_2$ solar cells and modules," *Thin Solid Films* **480,** 99 (2005).

21. S. Merdes, R. Sáez-Araoz, A. Ennaoui, J. Klaer, M. C. Lux-Steiner, and R. Klenk, "Recombination mechanisms in highly efficient thin film Zn(S,O)/Cu(In,Ga)S$_2$ based solar cells," *Appl. Phys. Lett.* **95,** 213502 (2009).

22. A. Ennaoui, M. Bär, J. Klaer, T. Kropp, R. Sáez-Araoz, and M. C. Lux-Steiner, "Highly-efficient Cd-free CuInS$_2$ thin-film solar cells and mini-modules with Zn(S,O)

buffer layers prepared by an alternative chemical bath process," *Prog. Photovolt: Res. Appl.* **14,** 499 (2006).

23. M. Gloeckler, "Device Physics of Cu(In,Ga)Se$_2$ Thin-Film Solar Cells," *Dissertation*, Colorado State University (2005).

24. A. Hagfeldt, G. Boschloo, L. Sun, L. Kloo, and H. Pettersson, "Dye-sensitized solar cells," *Chem. Rev.* **110,** 6595 (2010).

25. M. Grätzel, "Solar energy conversion by dye-sensitized photovoltaic cells," *Inorg. Chem.* **44,** 6841 (2005).

26. J. M. Kroon, N. J. Bakker, H. J. P. Smit, P. Liska, K. R. Thampi, P. Wang, S. M. Zakeeruddin, M. Grätzel, A. Hinsch, S. Hore, U. Würfe, R. Sastrawan, J. R. Durrant, E. Palomares, H. Pettersson, T. Gruszecki, J. Walter, K. Skupien, and G. E. Tulloch, "Nanocrystalline dye-sensitized solar cells having maximum performance," *Prog. Photovolt: Res. Appl.* **15,** 1 (2007).

27. B. O'Regan, and M. Grätzel, "A low-cost, high-efficiency solar cell based on dye-sensitized colloidal TiO$_2$ films," *Nature* **353,** 737 (1991).

28. A. Yella, H. W. Lee, H. N. Tsao, C. Yi, A. K. Chandiran, M. K. Nazeeruddin, E. W. G. Diau, C. Y. Yeh, S. M. Zakeeruddin, and M. Grätzel, "Porphyrin-sensitized solar cells with cobalt (II/III)-based redox electrolyte exceed 12 percent efficiency," *Science* **334,** 629 (2011).

29. J. Bisquert, D. Cahen, G. Hodes, S. Rühle, and A. Zaban, "Physical chemical principles of photovoltaic conversion with nanoparticulate, mesoporous dye-sensitized solar cells," *J. Phys. Chem. B* **108,** 8106 (2004).

Chapter 1

30. M. Grätzel, "Photoelectrochemical cells," *Nature* **414,** 338 (2001).

31. T. W. Hamann, R. A. Jensen, A. B. F. Martinson, H. Van Ryswyk, and J. T. Hupp, "Advancing beyond current generation dye-sensitized solar cells," *Energy Environ. Sci.* **1,** 66 (2008).

32. B. Gerrit, and H. Anders, "Characteristics of the iodide/triiodide redox mediator in dye-sensitized solar cells," *Acc. Chem. Res.* **42,** 1819 (2009).

33. T. P. Chou, Q. Zhang, and G. Cao, "Effects of dye loading conditions on the energy conversion efficiency of ZnO and TiO$_2$ dye-sensitized solar cells," *J. Phys. Chem. C* **111,** 18804 (2007).

34. K. Kalyanasundaram, and M. Grätzel, "Applications of functionalized transition metal complexes in photonic and optoelectronic devices," *Coord. Chem. Rev.* **177,** 347 (1998).

35. E. M. Kaidashev, M. Lorenz, H. Von Wenckstern, A. Rahm, H. C. Semmelhack, K. H. Han, G. Benndorf, C. Bundesmann, H. Hochmuth, and M. Grundmann, "High electron mobility of epitaxial ZnO thin films on c-plane sapphire grown by multistep pulsed-laser deposition," *Appl. Phys. Lett.* **82,** 3901 (2003).

36. H. Tang, K. Prasad, R. Sanjinès, P. E. Schmid, and F. Lévy, "Electrical and optical properties of TiO$_2$ anatase thin films," *J. Appl. Phys.* **75,** 2042 (1994).

37. M. Quintana, T. Edvinsson, A. Hagfeldt, and G. Boschloo, "Comparison of dye-sensitized ZnO and TiO$_2$ solar cells: Studies of charge transport and carrier lifetime," *J. Phys. Chem. C* **111,** 1035 (2007).

Chapter 2.

Post-Annealing Effects on the Structural and Optical Properties of Zn(S,O) Buffer Layer for Thin-Film Solar Cells

2.1. Introduction

Zn(S,O) buffer layer is one of the most studied buffer layer for replacing CdS, because it is non-toxic and has a large bandgap (3.6 eV). The research of the chemical bath deposited Zn(S,O) (CBD-Zn(S,O)) buffer layer started in the beginning of the 1990s [1]. However, the most important progress was made by Showa Shell in 1996 [2]. Since then, the new bath compositions of CBD-Zn(S,O) have been studied, all of them leading to very high efficiency of Cd free CIGS compared to their CdS references [3-6]. Although ZnS has advantages as mentioned above, the conversion efficiencies of CIGS solar cells fabricated using CBD-Zn(S,O) buffer layer have not exceeded those of the CIGS solar cells with CBD-CdS buffer layer [7,8].

There have been many attempts to get over this limitation. Platzer-Björkman's group reported Zn(O,S) buffer layer deposited by atomic layer deposition (ALD) method [9]. They measured efficiencies of CIGS solar cells with different sulfur concentrations of Zn(O,S) thin film. The trend in device performance was that the photocurrent was blocked for high sulfur concentration. On the other hand, when the sulfur concentration

was too low, V_{oc} was decreased. Both the loss of V_{oc} and the blocked photocurrent can be explained by the band alignment at the CIGS/Zn(O,S) interface. The band alignment strongly depends on the sulfur concentration [9,10]. Therefore, control of the S/O ratio in Zn(S,O) is important for improving the CIGS cell efficiency [11,12].

However, the ALD is a very slow process and not applicable to the industry. On the contrary, heat treatment is commonly used in semiconductor processing. Nair's group reported the decrease of sulfur amount in ZnS thin films confirmed by XRF when the chemical bath deposited ZnS thin films were oxidized in air annealing. [13]. However, the sulfur concentration was not measured quantitatively at each annealing temperature. Ennaoui's group observed optical bandgap decrease of CBD-ZnS thin films when annealed in argon atmosphere. [14]. But the reason of the bandgap change was not explained. In this point of view, we studied the effects of annealing temperature on the composition and optical bandgap of CBD-Zn(S,O). The sulfur ratio in Zn(S,O) was analyzed by EDX method, and increase amount of ZnO in thin films was confirmed using XPS. In addition, the function of the Zn(S,O) blocking layer for ZnO-based dye-sensitized solar cells was indentified with various Zn(S,O) deposition times.

2.2. Experiments

The Zn(S,O) thin films were deposited on thermally oxidized Si (001) or fused silica substrates by following the CBD method of Nakada's group with some modifications [3]. 0.15 M of zinc sulfate heptahydrate ($ZnSO_4 \cdot 7H_2O$), 0.6 M of

thiourea ($SC(NH_2)_2$), and 7 M of ammonium hydroxide (NH_4OH) aqueous solutions were mixed with stirring. The mixed solution was heated to 80°C. The cleaned substrates were vertically dipped in the solution for 23 min. After that, the substrates were taken out of the bath, rinsed with distilled water in order to remove the remained solution and dried using N_2 blower. To obtain the thick layer, this process was repeated for 8 times. The deposited samples were annealed in air at 200°C, 300°C, 400°C, and 500°C for one hour. The Zn(S,O) blocking layer was formed by CBD method on a fluorine-doped tin oxide substrate (FTO, TEC 8: Pilkington). The thickness of the blocking layer was controlled by changing the deposition time (10, 15, and 20 min). After then the DSSCs were fabricated using the Zn(S,O) blocking layer deposited on FTO. The method and procedure for fabricating DSSCs will be explained in chapter 3.

The nanostructural properties of the Zn(S,O) films were analyzed by x-ray diffraction (XRD, New D8 Advance: Bruker). The UV/Visible spectroscopy (Lambda 35: Perkin-Elmer) was used to measure absorption coefficient α, and the optical bandgap (E_g^{op}) was reckoned from the α^2 vs. hv (photon energy) plot. The surface morphology was observed with field emission-scanning electron microscopy (FE-SEM, SU70: Hitachi, Japan). The compositional analysis of the films was performed by energy-dispersive x-ray spectroscopy (FE-SEM/EDX, SU70: Hitachi). The chemical binding energy of the elements in the Zn(S,O) films was studied by x-ray photoelectron spectroscopy (XPS, AXIS-HIS: KRATOS). The photocurrent-voltage (J-V) curves were characterized with a solar cell measurement (K3000: McScience, Korea) under a solar simulator (Xenon lamp, air mass (AM) 1.5, 100 mW/cm^2).

2.3. Results and Discussion

Figure 2-1 shows the XRD patterns for Zn(S,O) thin films on oxidized Si (001) substrates with various annealing temperatures. The peak positions and intensities from the cubic ZnS (JCPDS #80-0020) and the hexagonal ZnO (JCPDS #36-1451) are shown as solid bars. The as-deposited Zn(S,O) thin film had a broad ZnS (111) peak, and post-annealed samples had ZnS (111), (220), and (311) peaks which can be identified as cubic zinc-blende structure. It is well known that cubic ZnS is stable at room temperature [15]. Also, the peak intensities increased with increasing annealing temperature, which means the enhanced crystallinity of annealed samples. The ZnO peak was not shown even after annealing, which may have resulted from the reason that the ZnO formed in Zn(S,O) thin films during annealing has amorphous phase. Similar XRD patterns were observed in Zn(S,O) films by several researchers [16,17].

The FE-SEM observation shows morphologies of the as-deposited, 300°C, and 500°C post-annealed Zn(S,O) buffer layer on oxidized Si (001), as shown in Fig 2-2. The Zn(S,O) nanoparticles that had various size distributions from 33 nm to 400 nm covered the substrate surface. The average sizes of nanoparticles were 320 nm, 390 nm, and 380 nm, respectively, for the as-deposited, 300°C, and 500°C annealed Zn(S,O) buffer layer. And the number of Zn(S,O) particles per unit area is 2.10 μm^{-2}, 2.42 μm^{-2}, and 2.75 μm^{-2}, respectively, for the as-deposited, 300°C, and 500°C annealed sample. By increasing annealing temperature, the size and density of Zn(S,O) particles are increased with increasing annealing temperature.
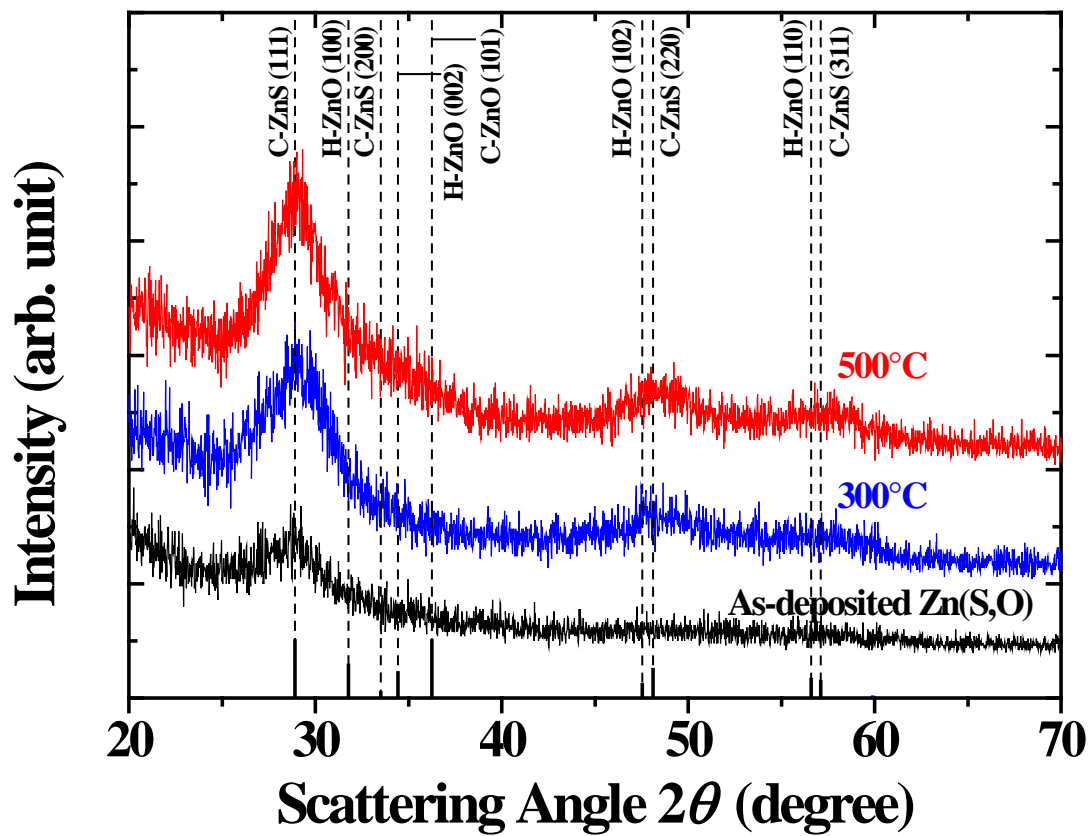
Fig. 2-1.   X-ray diffraction patterns of as-deposited and post-annealed Zn(S,O) buffer layer.   The peak positions and intensities from the cubic ZnS (C-ZnS, JCPDS #80-0020) and the hexagonal ZnO (H-ZnO, JCPDS #36-1451) are shown as solid bars.
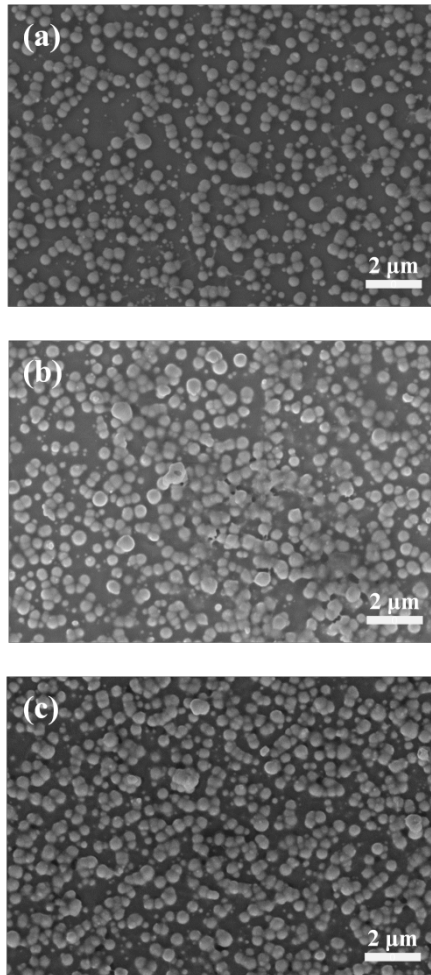
Fig. 2-2. Plan-view FE-SEM images of the (a) as-deposited, (b) 300°C, and (c) 500°C annealed Zn(S,O) buffer layer on oxidized Si (001).

The plots of α^2 vs. hv near the band edge for the Zn(S,O) films at various annealing temperatures are shown in Fig. 2-3. For a direct-bandgap semiconductor with parabolic band shape, the optical bandgap (E_g^{op}) is related to the photon energy hv by the Tauc's relation [18]:

$$\alpha^2 \propto (hv - E_g^{op}).\qquad(2\text{-}1)$$

Therefore, the optical bandgap was estimated from the α^2 vs. hv plot near the band edge. The E_g^{op} values of the as-deposited and annealed Zn(S,O) samples are summarized in Table 2-1. The optical bandgap values are decreased from 3.59 eV of as-deposited Zn(S,O) film to 2.97 eV of 500°C-annealed film. The reduced optical bandgap was due to the composition change of the Zn(S,O) films by the heat treatment [13,17,19]. The bandgap of Zn(S,O) films annealed in argon atmosphere was also decreased from 3.80 eV of as-deposited film to 2.99 eV of 500°C-annealed film [14]. The reason of bandgap change is sulfur evaporation and self-oxidation of the film. However, in this case possible oxidation agent is the remaining water in the film from the bath solution. The tendency of decreased bandgap was analogous to the result of air annealing, but the optical bandgap in each annealing temperature was different from air annealing sample. Similar result has been observed for chemical bath deposited CdS films annealed in argon atmosphere [20]. The 3.59 eV of as-deposited Zn(S,O) matched the literature value for cubic ZnS bandgap (3.6 eV). However, the bandgap of post-annealed samples except 200°C annealed sample had lower bandgap values (3.09 - 2.97 eV) than both of cubic ZnS (3.6 eV) and wurtzite ZnO (3.2 eV). This phenomenon can be explained by bandgap bowing. The bandgap of Zn(S,O) did not change linearly with a composition

change. Several researchers observed the bandgap bowing of the $ZnO_{1-x}S_x$ thin films [15,21,22]. But the bandgap of CBD-Zn(S,O) thin films was larger than sputter deposited $ZnO_{1-x}S_x$ films with the same composition, as shown in Table 2-1. The chemical bath deposited Zn(S,O) thin films contained H_2O and $Zn(OH)_2$ which came from the bath solution, so the composition of Zn, S, and O was different from sputter deposited Zn(S,O) thin films In the previous works, the bandgap change of the $ZnO_{1-x}S_x$ alloy was estimated by single fitting line [15,22]. However, the $ZnO_{1-x}S_x$ alloy had phase separation region composed of wurtzite and cubic structure, so the bandgap change can not be explained by just one fitting line. This result is contradictory to $Mg_xZn_{1-x}O$ alloy [23] and should be supplemented with more detailed studies.
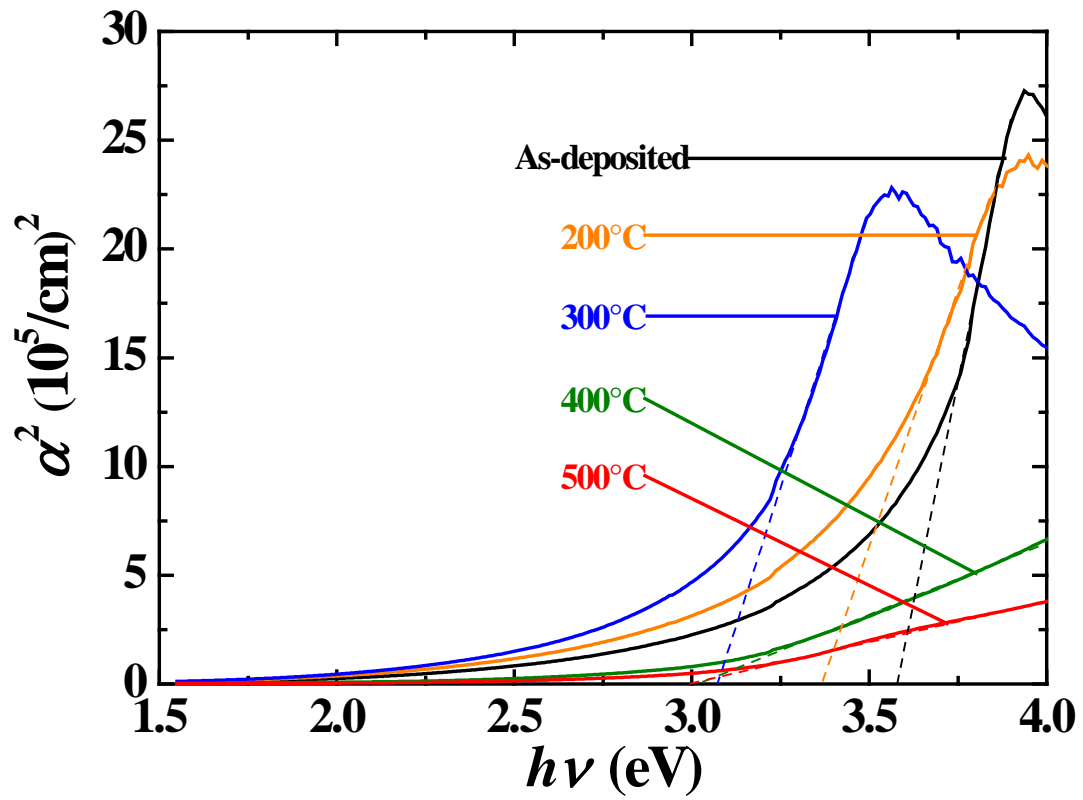
Fig. 2-3.   A plot of α^2 vs. $h\nu$ near the band edge for as-deposited and post-annealed Zn(S,O) thin films with various annealing temperatures.   The dotted lines represent the fit of the optical bandgap energy.

Table 2-1.   Optical bandgap of the as-deposited and post-annealed Zn(S,O) at different annealing temperatures.   The optical bandgap of sputter deposited $ZnO_{1-x}S_x$ thin films at the same composition is listed for comparison [15,22].

	As-deposited ($ZnO_{0.4}S_{0.6}$)	200°C	300°C ($ZnO_{0.47}S_{0.53}$)	400°C	500°C ($ZnO_{0.53}S_{0.47}$)
E_g^{op}	3.59 eV	3.37 eV	3.09 eV	3.04 eV	2.97 eV
E_g^{op} [15]	2.61 eV		2.58 eV		2.56 eV
E_g^{op} [22]	2.82 eV		2.77 eV		2.75 eV

The zinc, sulfur, and oxygen compositions of as-deposited and post-annealed Zn(S,O) buffer layers are shown in Table 2-2.   The EDX analysis was used to identify the composition of the Zn(S,O) thin films.   In this results, the sulfur ratio in Zn(S,O) films decreased with increasing the post-annealing temperature from 300°C to 500°C. The decreasing of S/Zn ratio can be explained by following chemical reaction [13]:

$$ZnS + 3/2O_2 \rightarrow ZnO + SO_2\uparrow. \tag{2-2}$$
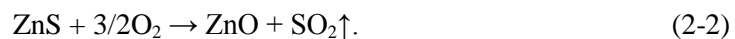
Sulfur of ZnS was oxidized by atmospheric oxygen and sublimated during the post-annealing.   However, the as-deposited Zn(S,O) had larger oxygen atomic percent than 300°C annealed sample.   It was caused by the formation of ZnO, $Zn(OH)_2$, and H_2O during the CBD process as follows: $Zn^{2+} + 2OH^- \leftrightarrow Zn(OH)_2$ (solid), $Zn(OH)_2 \leftrightarrow ZnO + H_2O$ [4,24].   The H_2O evaporated by a thermal energy during the post-annealing process, so the S/S+O ratio increased from 0.43 to 0.49.   The analytical precision and accuracy in EDX measurements are $\pm$ 1 - 2% and the quantitative analysis of oxygen by EDX is difficult [25].   For more accurate measurement, CHNS and ICP analysis were tried, but these instruments had practical limit to analyze Zn(S,O) thin films.   It is difficult to make enough amount of Zn(S,O) sample by CBD method for CHNS analysis.   And the exact amount of sulfur is not measured by ICP-AES, because the instrument can not precisely detect an anion.

The core levels (Zn $2p_{3/2}$, S $2p_{1/2}$, S $2p_{3/2}$, and O $1s$) of bare and post-annealed ZnO are shown in Fig. 2-4.   Each dashed line indicates the binding energy of the ZnS and ZnO deposited by CBD method [26-29].   Because the binding energies of the ZnS and ZnO are too close, the binding-energy shift of the Zn $2p$ core level between the bare

and annealed sample was not observed. However, by comparing the O 1s binding energy of the ZnO and ZnOH, the relative intensity of ZnO to ZnOH increased with annealing temperature. From this result, the composition change of the Zn(S,O) thin films by post-annealing was confirmed once again. The XPS spectra indicated sulfur still remained after 500°C annealing.

Table 2-2. Compositions of as-deposited and post-annealed Zn(S,O) buffer layers.

	Zn at. %	S at. %	O at. %	[S]/[S]+[O]	[S]/[Zn]
As-deposited	42	24	32	0.43	0.60
300°C	47	25	26	0.49	0.53
500°C	45	21	33	0.39	0.47
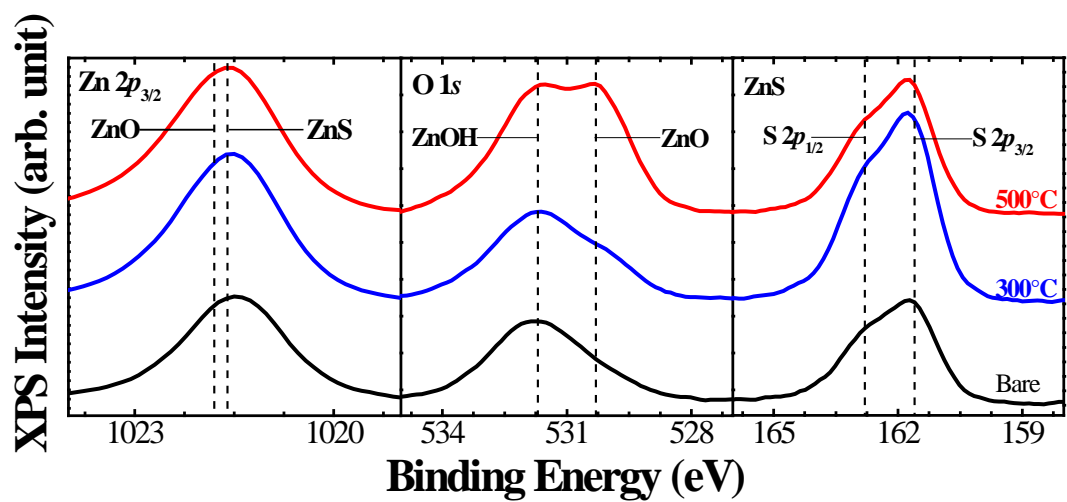
Fig. 2-4. XPS spectra of Zn $2p_{3/2}$ for ZnS and ZnO, O $1s$ for ZnO and ZnOH, and S $2p_{3/2}$ and S $2p_{1/2}$ for ZnS with various annealing temperature. The binding energies of chemical bath deposited ZnS and ZnO are shown as dashed lines [26-29].

Figure 2-4 shows the surface morphologies of the bare FTO substrate and Zn(S,O) thin films by FE-SEM. These Zn(S,O) thin films were deposited for blocking layer of DSSCs. The FTO substrates were covered by Zn(S,O) in 2 times deposited sample, but 100 nm-sized nanoparticles were observed in 4 times deposited sample.

From the *J-V* curves of the DSSCs in Fig. 2-5, the Zn(S,O) blocking layer depleted the short-circuit current (J_{sc}). As the blocking layer became thicker, J_{sc} gradually decreased. However, the open-circuit voltage (V_{oc}) of the cells with blocking layer did not show big difference from the bare cell. The photovoltaic properties for all cells are summarized in Table 2-3. The decreased power-conversion efficiency results by the CBD-Zn(S,O) blocking layer didn't match up with the electrodeposited and thermal evaporated ZnS [30]. One possible reason is that the Zn(S,O) blocking layer prohibits the injection of electron from ZnO to FTO, because of high resistivity (over 10^5 Ω cm) [31] and thick layer of CBD-Zn(S,O). For sputter deposited Nb_2O_5 blocking layer, the optimum thickness was just 5 nm with homogeneous coverage [32]. However, CBD-Zn(S,O) blocking layer had about 10 nm thickness for 10 min deposition. This is too thick for the electron injection, so the blocking layer will result the decrease of the short-circuit current.

``
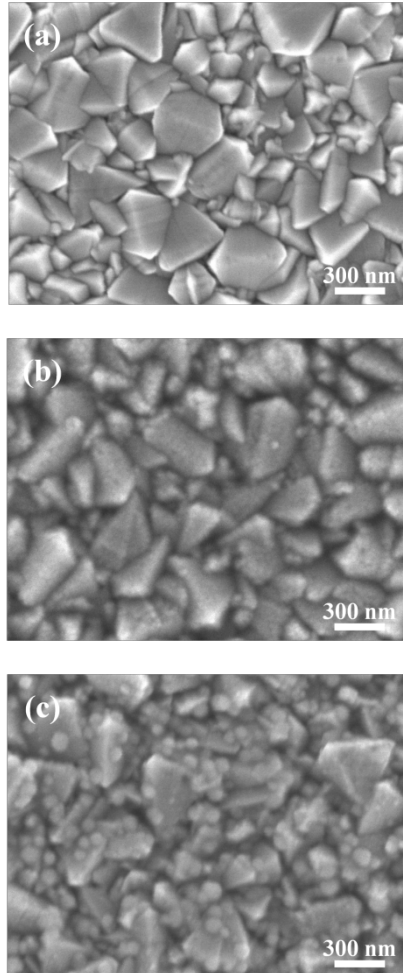
Fig. 2-5.   Plan-view FE-SEM images of (a) bare FTO electrode, and Zn(S,O) blocking layer coated on FTO electrode with different deposition times of (b) 2 times, and (c) 4 times.
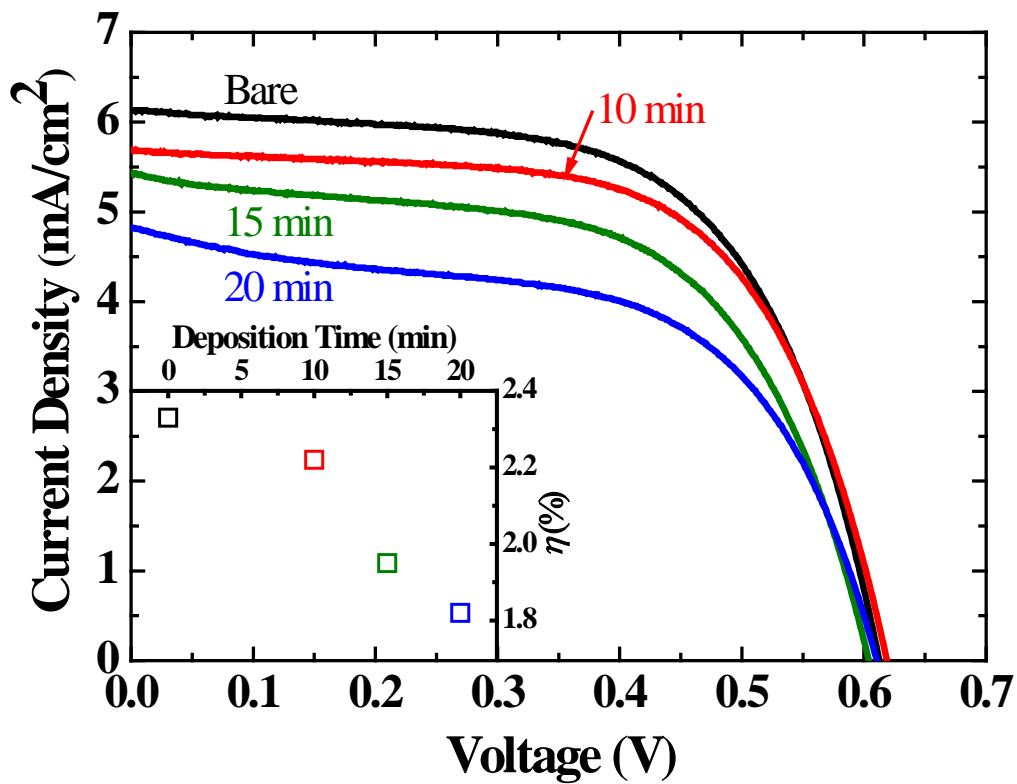
Fig. 2-6. Photocurrent-voltage curves of DSSCs with various Zn(S,O) blocking layer deposited times. The inset shows power-conversion efficiency of DSSCs as a function of the blocking layer deposition time.

Table 2-3.   Short-circuit current (J_{sc}), open-circuit voltage (V_{oc}), fill factor (FF), and power-conversion efficiency (η) of the DSSCs with and without blocking layer.

	J_{sc} (mA/cm^2)	V_{oc} (V)	FF	η
Bare	6.13	0.613	62.0%	2.33%
10 min	5.69	0.619	63.0%	2.22%
15 min	5.44	0.604	59.0%	1.94%
20 min	4.89	0.616	60.4%	1.82%

2.4. Conclusions

The effects of post-annealing temperature on the structural and optical properties of CBD-Zn(S,O) buffer layers were studied.   The chemical bath deposited Zn(S,O) thin films had a cubic zinc-blende structure with a poor crystallinity.   As increasing the annealing temperature, the crystallinity of Zn(S,O) thin films was increasing.   The optical bandgap value decreased from 3.59 eV of as-deposited Zn(S,O) film to 2.97 eV of 500°C-annealed film.   In addition, the bandgap bowing phenomenon was observed during the bandgap change of Zn(S,O) buffer layers.   This optical bandgap narrowing was correlated with the composition change of films by post-annealing.   The atomic percent of sulfur in Zn(S,O) buffer layers was decreased with increasing the post-annealing temperature from 300°C to 500°C.   The CBD-Zn(S,O) thin film applied to DSSCs blocking layer diminished the power-conversion efficiency.   If the thickness of the Zn(S,O) blocking layer is decreased by reducing the deposition time or diluting the concentration of the bath, the blocking layer will improve the short-circuit current of the DSSCs.

2.5. References

1. J. Kessler, M. Ruckh, D. Hariskos, U. Ruhle, R. Menner, and H. W. Schock, "Interface engineering between CuInSe$_2$ and ZnO," *Photovoltaic Specialists Conference, 1993., Conference Record of the Twenty Third IEEE* 447 (1993).

2. K. Kushiya, T. Nii, I. Sugiyama, Y. Sato, Y. Inamori, and H. Takeshita, "Application of Zn-compound buffer layer for polycrystalline CuInSe$_2$-based thin-film solar cells," *Jpn. J. Apl. Phys.,Part 1* **35,** 4383 (1996).

3. T. Nakada, and M. Mizutani, "18% efficiency Cd-free Cu(In,Ga)Se$_2$ thin-film solar cells fabricated using chemical bath deposition (CBD)-ZnS buffer layers," *Jpn. J. Apl. Phys.,Part 2* **41,** L165 (2002).

4. T. Nakada, K. Furumi, and A. Kunioka, "High-efficiency cadmium-free Cu(In,Ga)Se$_2$ thin-film solar cells with chemically deposited ZnS buffer layers," *IEEE T. Electron. Dev.* **46,** 2093 (1999).

5. T. Nakada, M. Mizutani, Y. Hagiwara, and A. Kunioka, "High-efficiency Cu(In,Ga)Se$_2$ thin-film solar cells with a CBD-ZnS buffer layer," *Sol. Energy Mater. Sol. Cells* **67,** 255 (2001)

6. A. Ennaoui, S. Siebentritt, M. C. Lux-Steiner, W. Riedl, and F. Karg, "High-efficiency Cd-free CIGSS thin-film solar cells with solution grown zinc compound buffer layers," *Sol. Energy Mater. Sol. Cells* **67,** 31 (2001).

7. I. Repins, M. A. Contreras, B. Egaas, C. DeHart, J. Scharf, C. L. Perkins, B. To, and R. Noufi, "19.9%-efficient ZnO/CdS/CuInGaSe$_2$ solar cell with 81.2% fill factor," *Prog. Photovolt: Res. Appl.* **16,** 235 (2008).

8. T. N. M.A. Contreras, M. Hongo, "ZnO/ZnS(O,OH)/Cu(In,Ga)Se$_2$/Mo SOLAR CELL WITH 18.6% EFFICIENCY," *3rd World Conference on Photovoltaic Energy Conversion* 570 (2003).

9. C. Platzer-Bjorkman, T. Torndahl, D. Abou-Ras, J. Malmstrom, J. Kessler, and L. Stolt, "Zn(O,S) buffer layers by atomic layer deposition in Cu(In,Ga)Se$_2$ based thin film solar cells: Band alignment and sulfur gradient," *J. Appl. Phys.* **100,** 044506 (2006).

10. T. Nakada, M. Hongo, and E. Hayashi, "Band offset of high efficiency CBD-ZnS/CIGS thin film solar cells," *Thin Solid Films* **431,** 242 (2003).

11. A. Yamada, K. Matsubara, K. Sakurai, S. Ishizuka, H. Tampo, P. J. Fons, K. Iwata, and S. Niki, "Effect of band offset on the open circuit voltage of heterojunction CuIn$_{1-x}$Ga$_x$Se$_2$ solar cells," *Appl. Phys. Lett.* **85,** 5607 (2004).

12. A. Niemegeers, M. Burgelman, and A. Devos, "On The CdS/CuInSe$_2$ Conduction-Band Discontinuty," *Appl. Phys. Lett.* **67,** 843 (1995).

13. O. L. Arenas, M. T. S. Nair, and P. K. Nair, "Chemical bath deposition of ZnS thin films and modification by air annealing," *Semicond. Sci. Technol.* **12,** 1323 (1997).

14. S. D. Sartale, B. R. Sankapal, M. Lux-Steiner, and A. Ennaoui, "Preparation of nanocrystalline ZnS by a new chemical bath deposition route," *Thin Solid Films* **480-481,** 168 (2005).

15. B. K. Meyer, A. Polity, B. Farangis, Y. He, D. Hasselkamp, T. Krämer, and C. Wang, "Structural properties and bandgap bowing of ZnO1-x Sx thin films deposited by reactive sputtering," *Appl. Phys. Lett.* **85,** 4929 (2004).

16. S. H. Mohamed, M. El-Hagary, and M. Emam-Ismail, "Thickness and annealing effects on the optoelectronic properties of ZnS films," *J. Phys. D: Appl. Phys.* **43,** (2010).

17. S. W. Shin, H. P. Oh, S. M. Pawar, J. H. Moon, and J. H. Kim, "Effect of complexing agent and annealing atmosphere on properties of nanocrystalline ZnS thin films," *J. Nanosci. Nanotechnol.* **10,** 3686 (2010).

18. Y. Kim, W. Lee, D. R. Jung, J. Kim, S. Nam, H. Kim, and B. Park, "Optical and electronic properties of post-annealed ZnO:Al thin films," *Appl. Phys. Lett.* **96,** (2010).

19. L. Zhou, Y. Xue, and J. Li, "Study on ZnS thin films prepared by chemical bath deposition," *Journal of Environmental Sciences* **21,** S76 (2009).

20. H. Metin and R. Esen, "Annealing effects on optical and crystallographic properties of CBD grown CdS films," *Semicond. Sci. Technol.* **18,** 647 (2003).

21. C. Persson, C. Platzer-Bjorkman, J. Malmstrom, T. rndahl, and M. Edoff, "Strong Valence-Band Offset Bowing of $ZnO_{1-x}S_x$ Enhances p-Type Nitrogen Doping of ZnO-like Alloys," *Phys. Rev. Lett.* **97,** 146403 (2006).

22. H. L. Pan, T. Yang, B. Yao, R. Deng, R. Y. Sui, L. L. Gao, and D. Z. Shen, "Characterization and properties of $ZnO_{1-x}S_x$ alloy films fabricated by radio-frequency magnetron sputtering," *Appl. Surf. Sci.* **256,** 4621 (2010).

23. H. Morkoç and Ü. Özgür, Zinc Oxide: Fundamentals, Materials and Device Technology, (Wiley, Weinheim, 2009), pp. 352-359.

24. A. Goudarzi, G. M. Aval, S. S. Park, M. C. Choi, R. Sahraei, M. H. Ullah, A. Avane,

and C. S. Ha, "Low-Temperature Growth of Nanocrystalline Mn-Doped ZnS Thin Films Prepared by Chemical Bath Deposition and Optical Properties," *Chem. Mater.* **21,** 2375 (2009).

25. J. Goldstein, D. Newbury, D. Joy, C. Lyman, P. Echlin, E. Lifshin, L. Sawyer, and J. Michael, Scanning Electron Microscopy and X-ray Microanalysis, 3rd ed., (Springer Science, New York, 2003), pp. 391-394.

26. M. Ahmad, X. Yan, and J. Zhu, "Controlled synthesis, structural evolution, and photoluminescence properties of nanoscale one-dimensional hierarchical ZnO/ZnS heterostructures," *J. Phys. Chem. C* **115,** 1831 (2011).

27. M. Bar, A. Ennaoui, J. Klaer, T. Kropp, R. Saez-Araoz, N. Allsop, I. Lauermann, H. W. Schock, and M. C. Lux-Steiner, "Formation of a ZnS/Zn(S,O) bilayer buffer on CuInS$_2$ thin film solar cell absorbers by chemical bath deposition," *J. Appl. Phys.* **99,** 123503 (2006).

28. H. Khallaf, G. Chai, O. Lupan, H. Heinrich, S. Park, A. Schulte, and L. Chow, "Investigation of chemical bath deposition of ZnO thin films using six different complexing agents," *J. Phys. D: Appl. Phys.* **42,** 135304 (2009).

29. J. Ouerfelli, M. Regragui, M. Morsli, G. Djeteli, K. Jondo, C. Amory, G. Tchangbedji, K. Napo, and J. C. Bernède, "Properties of ZnO thin films deposited by chemical bath deposition and post annealed," *J. Phys. D: Appl. Phys.* **39,** 1954 (2006).

30. J. Y. Liao, and K. C. Ho, "A photovoltaic cell incorporating a dye-sensitized ZnS/ZnO composite thin film and a hole-injecting PEDOT layer," *Sol. Energy Mater. Sol. Cells* **86,** 229 (2005).

31. S. W. Shin, G. L. Agawane, M. G. Gang, A. V. Moholkar, J. H. Moon, J. H. Kim, and J. Y. Lee, "Preparation and characteristics of chemical bath deposited ZnS thin films: Effects of different complexing agents," *J. Alloys Compd.* **526,** 25 (2012).

32. J. Xia, N. Masaki, K. Jiang, and S. Yanagida, "Sputtered Nb_2O_5 as a novel blocking layer at conducting glass/TiO_2 interfaces in dye-sensitized ionic liquid solar cells," *J. Phys. Chem. C* **111,** 8092 (2007).

Chapter 2

Chapter 3.

The Effect of Al Doping on the Performance in Nanoporous ZnO-Based Dye-Sensitized Solar Cells

3.1. Introduction

Dye-sensitized solar cells (DSSCs) have been considered as one of the potential candidates for next-generation solar cells due to their low cost, high durability, large flexibility in shape, various colors, and transparency. The DSSCs have enormous progress since 1991 [1]. The maximum efficiency of 11% and lifetime of 10,000 h have been achieved [2].

The photoelectrode is one of the important components in DSSCs. For photoelectrode material, large surface area that sufficient dye molecules can be absorbed and the suitable energy levels are required for getting high power-conversion efficiency. TiO_2 is the commonly used oxide semiconductor for photoelectrode material, but ZnO has a high potential to be used as a photoelectrode material. The main reasons are that ZnO has similar direct bandgap (~3.2 eV) and the band edges position to those of anatase TiO_2, and the carrier mobility of single-crystal ZnO (115 - 155 cm^2/Vs) is much higher than TiO_2 (1 - 4 cm^2/Vs) [3,4]. Furthermore, various ZnO nanostructures can be made by facile and low-cost techniques [5]. In spite of these advantages, the power-

conversion efficiency of ZnO-based DSSCs is much lower (7.5%) than that of TiO_2 solar cells (12.3%) [6,7].

In this research, we synthesized the micrometer-sized polydispersed ZnO aggregates made up of nanoparticles using a hydrolysis method. In the hierarchical photoanode, micron-size aggregates can improve photon absorption by increase of light scattering, and supply extensive internal surface area needed for high dye loading. Many researchers have reported that the addition of large-sized particles as light scatterers enhances the optical absorption due to the lengthened travelling distance of the incident light [8-10]. For that reason, the generation of electron-hole pairs is enhanced. However, these structures reduce the specific surface area and increase the recombination rate because of the extended the path lengths of the electrons. However, nanoporous ZnO aggregates lead effective light scattering without loss of the specific surface area for dye loading [7].

Doping is commonly used method for change the electrical property of a semiconductor. Several materials such as Al, Sn, I, F, and Li have been reported as doping material on ZnO-based DSSCs [11-14]. Among these materials, Al has been considered as one of the typical dopants for forming an n-type ZnO with good optical quality, low resistivity, and high conductance [15]. It was found that the Al doping improves the power-conversion efficiency of DSSCs composed of ZnO nanorod and nanofiber [14,16,17]. However, these DSSCs have too low efficiency. Therefore, in our research, Al doped ZnO aggregates (denoted as ZnO:Al) fabricated by a hydrolysis method and photovoltaic properties are systematically identified with various Al doping

concentrations.

3.2. Experiments

For the fabrication of polydispersed ZnO and Al doped ZnO aggregates, zinc acetate dihydrate ($Zn(CH_3COO)_2 \cdot 2H_2O$) and aluminum acetate ($Al(OH)(C_2H_3O_2)_2$) were added to diethylene glycol ($C_4H_{10}O_3$) and heated in autoclave at 160°C for 6 h. The concentrations of Al in the solution are 0.1 and 0.5 at. %. Then, the as-synthesized solution was centrifuged at 3000 rpm for 30 min to separate the aggregates from solvent. The precipitates were redispersed in ethanol and centrifuged again, and then it was dried in the oven at 60°C. In order to fabricate viscous paste, 1 g of as-synthesized ZnO or ZnO:Al powder, 0.6 g of cellulose and 7 ml terpineol were prepared, and these mixtures were stirred for a day to make the homogeneous paste [35]. The pastes were smoothed on a fluorine-doped tin oxide substrate (FTO, TEC 8: Pilkington) by a one-step doctor-blade method. The active area of the photoelectrode was 0.1256 cm^2, and the thickness of the ZnO aggregates layer was approximately 12 µm. The as-deposited films were annealed at 350°C for 1 hour in air to evaporate any residual organic solvent and enhance the necking between ZnO particles. For dye adsorption, the deposited films were immersed in 0.5 mM anhydrous ethanol solution of N719 dye ($RuL_2(NCS)_2$:2TBA, L = 2,2$^{'}$-bipyridyl-4,4$^{'}$-dicarboxylic acid, TBA = tetrabutylammonium: Solaronix) for 30 min at room temperature. The Pt was deposited on the FTO substrate, served as counter electrode, by rf-magnetron sputtering. A thermoplastic foil (25 µm: Dupont, France) stuck the dye-adsorbed ZnO or ZnO:Al electrode and Pt counter electrode, and an iodide-

based redox electrolyte (AN-50: Solaronix) was injected into the gap between the two electrodes.

X-ray diffraction (XRD, New D8 Advance: Bruker) was used for characterizing structural properties of the ZnO electrode. The photocurrent-voltage (J-V) curves were characterized with a solar cell measurement system (K3000: McScience, Korea) under a solar simulator (Xenon lamp, air mass (AM) 1.5, 100 mW/cm^2). The surface morphology was observed with field emission-scanning electron microscopy (FE-SEM, SU70: Hitachi, Japan).

3.3. Results and Discussion

Figure 3-1 shows the J-V curves for bare and Al doped ZnO-DSSCs with various doping concentration. As the Al doping concentration became higher, the open-circuit voltage (V_{oc}) and short-circuit current (J_{sc}) gradually decreased. Consequently, the power-conversion efficiency decreased with increasing Al doping concentration. This result is contrary to the results of the Li or I doped ZnO-aggregates DSSCs [12,13]. The photovoltaic properties are summarized in Table 3-1.

To explain the reason of the decreased power-conversion efficiency, the changes of structural properties with various Al doping concentrations were analyzed by x-ray diffraction (Fig. 3-2). The peak positions and intensities from the hexagonal ZnO (JCPDS #36-1451) are shown as solid bars. The SnO peaks were originated from the FTO substrate. The ZnO and ZnO:Al nanoparticles had a hexagonal wurtzite structure, with no secondary phase. The grain size and local strain of ZnO and ZnO:Al

nanocrystals were determined from the Williamson-Hall plot [18,19].

The power-conversion efficiency, grain size, and local strain of ZnO nanoparticles are shown as a function of Al doping concentration in Fig. 3-3. The grain size of ZnO increased from 33 nm to 41 nm by 0.1 atomic percent doping, and other researchers also obtained this tendency [20,21]. In general, as the grain size of the semiconductor oxide increases, the specific surface area for dye adsorption decreases [22]. For this reason, the short-circuit current density of the ZnO:Al-based DSSCs was decreased [23]. The local strain of ZnO also increased from 0.24% (bare) to 0.41% (0.5 at. % Al doping). The local strain increment may be contributed to the increased defects caused by the Al dopants which are located at the ZnO interstitial site. As a result, these defects act as recombination center of electron-hole pairs and interrupt the movement of carriers [24,25]. Therefore, the power-conversion efficiencies of the ZnO:Al-based DSSCs decrease.

Figure 3-4 shows the plan-view FE-SEM images of ZnO with and without Al doping. It can be seen that the morphology of bare ZnO is micrometer-sized aggregates consisting of nanoparticles, but the ZnO:Al is nanometer-sized aggregates consisting of nanorods. The result that diameter of nanorod was bigger than nanoparticles was consistent with the grain size increase obtained from XRD. The nanorod will greatly decrease the surface area for dye adsorption and it may cause decreased short-circuit current. It was previously reported that the Al dopant affects the morphology of ZnO. Lim's group reported morphology change of the ZnO nanorod by Al doping [16]. The Al dopant decreased the diameter of nanorod from 100 nm to 50 nm and changed the

shape of nanorod. In addition, the Al doped ZnO nanorod arrays were denser than undoped sample, and the denser structure caused the surface increase for dye loading. Waki's group observed morphology change with various Al doping concentration [14]. The diameter and length of the ZnO nanorod were increased at 0.5 at. % Al doping sample, but they were decreased at 2.5 and 5 at. % Al doping sample. The sample of 0.25 at. % Al doping had the smallest dye loading amount, because average diameter was about twice as large as others.
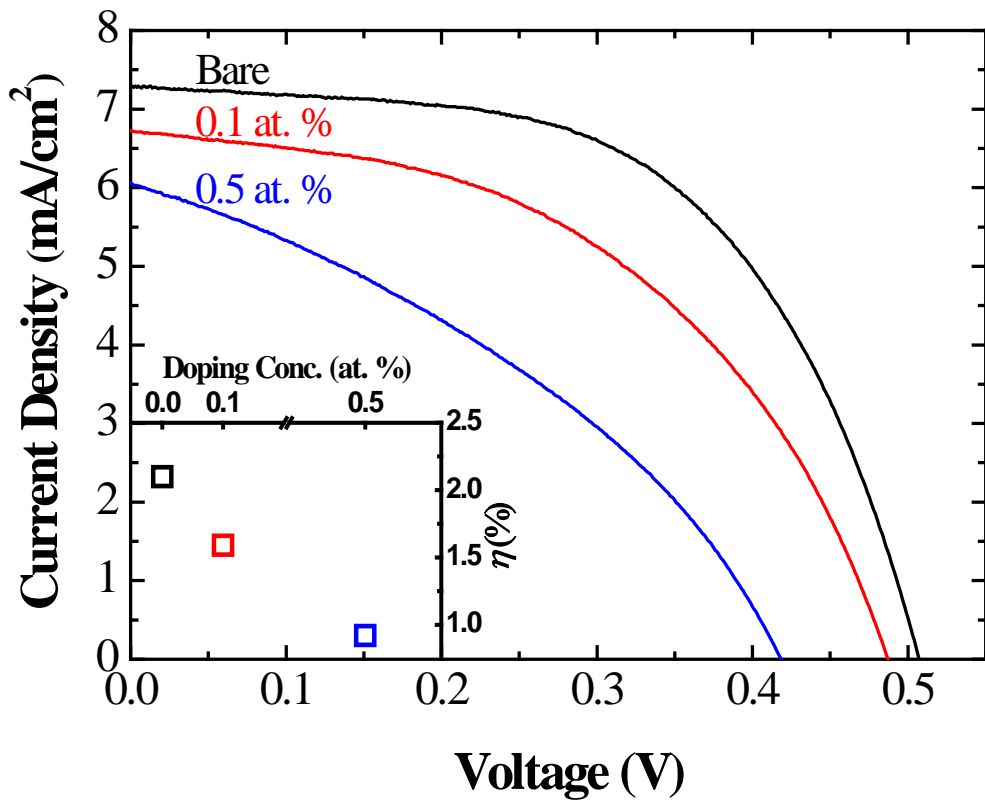
Fig. 3-1.   Photocurrent-voltage curves of DSSCs with various Al doping concentrations. The inset shows power-conversion efficiency of DSSCs as a function of the Al doping concentration.

Table 3-1. Short-circuit current (J_{sc}), open-circuit voltage (V_{oc}), fill factor (*FF*), and power-conversion efficiency (η) of the DSSCs with and without Al doping.

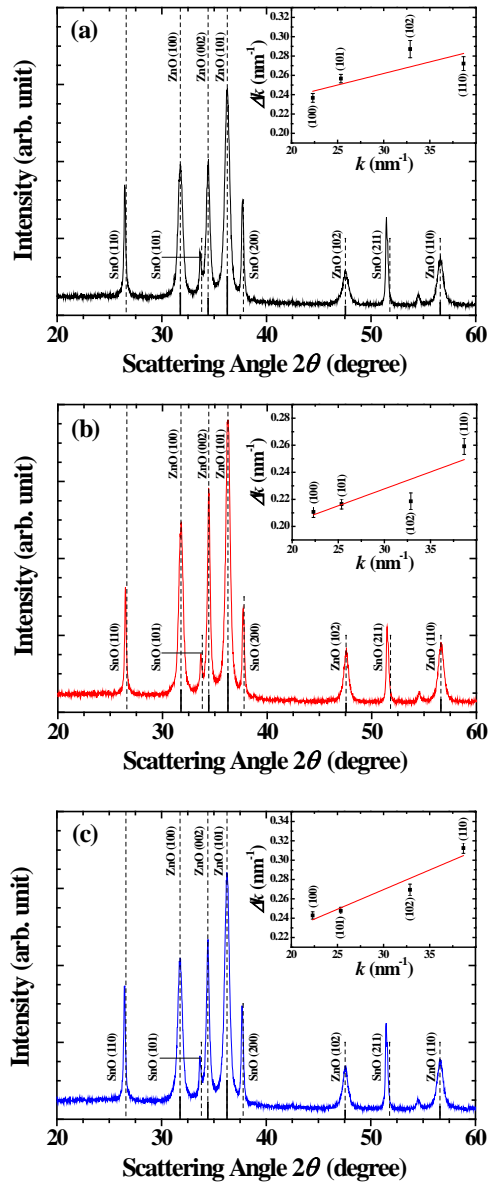|	J_{sc} (mA/cm^2)	V_{oc} (V)	*FF*	η
Bare	7.29	0.507	56.8%	2.10%
0.1 at. %	7.07	0.474	47.4%	1.59%
0.5 at. %	6.06	0.418	36.3%	0.92%

Fig. 3-2. X-ray diffraction of the (a) bare ZnO, (b) 0.1 at. % ZnO:Al, and (c) 0.5 at. %
ZnO:Al thin films on FTO after annealing at 350°C.   The peak intensities and positions
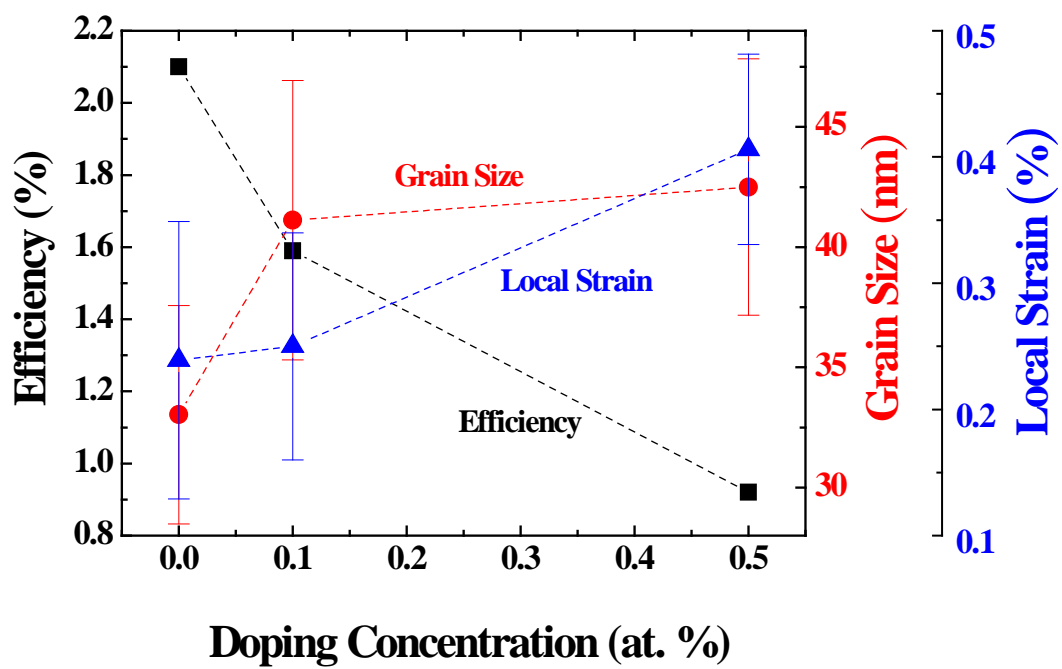from the hexagonal ZnO (JCPDS #36-1451) are shown as solid bars.

Fig. 3-3.   Efficiency, Grain Size, and Local Strain of ZnO and ZnO:Al as a function of doping concentration.
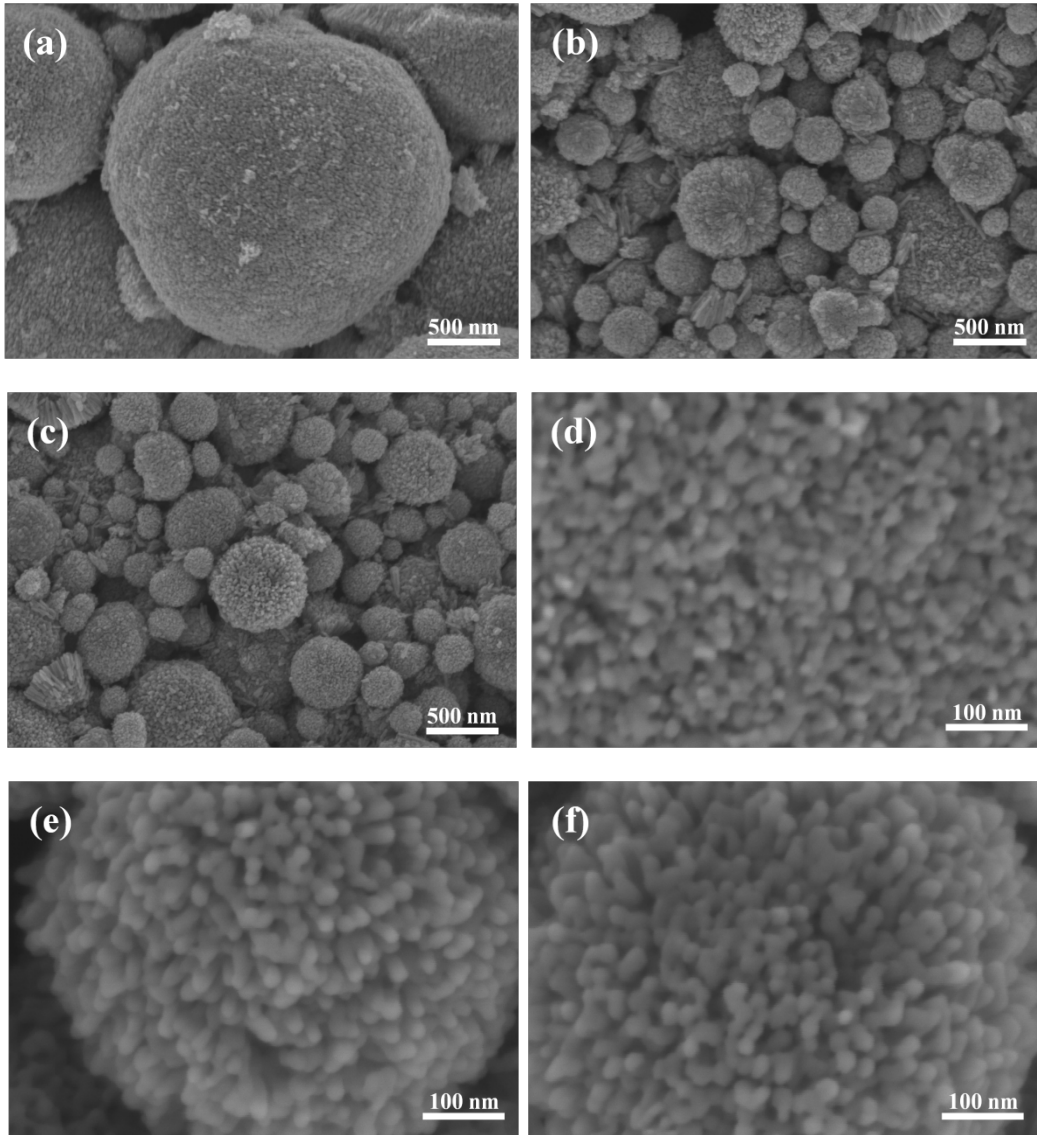
Fig. 3-4.   Plan-view FE-SEM images of (a) bare, (b) 0.1 at. % ZnO:Al, and (c) 0.5 at. %

ZnO:Al thin films on FTO after annealing at 350°C.   Magnified images of (d) bare, (e)

0.1 at. % ZnO:Al, and (f) 0.5 at. % ZnO:Al.

3.4. Conclusions

Micormeter-sized polydispersed Al doped ZnO aggregates made up of nanoparticles were synthesized by a hydrolysis method for photoelectrodes in dye-sensitized solar cells. In the hierarchical photoanode, micron-size aggregates can improve photon absorption by increasing the light scattering, and supply extensive internal surface area needed for high dye loading. However, the Al doping on ZnO aggregates lessened the open-circuit voltage (V_{oc}) and short-circuit current (J_{sc}). As a result, the power-conversion efficiency decreased by Al doping. The local strain and grain size of ZnO aggregates were increased with increasing doping concentration. The increased grain size caused the decreased specific surface area for dye adsorption, and it may cause the decreased open-circuit voltage. The rise of local strain was evidence of the increased defect density by Al doping. Defects act as recombination center and interrupt the movement of carriers. Also, the morphology and aggregate size change through Al doping was confirmed by FE-SEM. The size of nanorods was much bigger than nanoparticles of bare ZnO. It was a definite evidence for decreased surface area. For these negative effects, the power-conversion efficiencies of ZnO:Al-based DSSCs were decreased. The amount of adsorbed dye with various Al doping concentrations can be carried out by desorbing the dye from the ZnO films to the NaOH solution and then measured from the ultraviolet-visible absorption spectra of the resultant solution. If the Al doping concentration is reduced to the condition that does not show morphology change of ZnO, the power-conversion efficiency will be increased.

3.5. References

1. B. O'Regan, and M. Grätzel, "A low-cost, high-efficiency solar cell based on dye-sensitized colloidal TiO_2 films," *Nature* **353,** 737 (1991).

2. J. M. Kroon, N. J. Bakker, H. J. P. Smit, P. Liska, K. R. Thampi, P. Wang, S. M. Zakeeruddin, M. Grätzel, A. Hinsch, S. Hore, U. Würfe, R. Sastrawan, J. R. Durrant, E. Palomares, H. Pettersson, T. Gruszecki, J. Walter, K. Skupien, and G. E. Tulloch, "Nanocrystalline dye-sensitized solar cells having maximum performance," *Prog. Photovolt: Res. Appl.* **15,** 1 (2007).

3. E. M. Kaidashev, M. Lorenz, H. Von Wenckstern, A. Rahm, H. C. Semmelhack, K. H. Han, G. Benndorf, C. Bundesmann, H. Hochmuth, and M. Grundmann, "High electron mobility of epitaxial ZnO thin films on c-plane sapphire grown by multistep pulsed-laser deposition," *Appl. Phys. Lett.* **82,** 3901 (2003).

4. H. Tang, K. Prasad, R. Sanjinès, P. E. Schmid, and F. Lévy, "Electrical and optical properties of TiO_2 anatase thin films," *J. Appl. Phys.* **75,** 2042 (1994).

5. M. Quintana, T. Edvinsson, A. Hagfeldt, and G. Boschloo, "Comparison of dye-sensitized ZnO and TiO_2 solar cells: Studies of charge transport and carrier lifetime," *J. Phys. Chem. C* **111,** 1035 (2007).

6. A. Yella, H. W. Lee, H. N. Tsao, C. Yi, A. K. Chandiran, M. K. Nazeeruddin, E. W. G. Diau, C. Y. Yeh, S. M. Zakeeruddin, and M. Grätzel, "Porphyrin-sensitized solar cells with cobalt (II/III)-based redox electrolyte exceed 12 percent efficiency," *Science* **334,** 629 (2011).

7. N. Memarian, I. Concina, A. Braga, S. M. Rozati, A. Vomiero, and G. Sberveglieri,

"Hierarchically assembled ZnO nanocrystallites for high-efficiency dye-sensitized solar cells," *Angew. Chem. Int. Ed.* **50,** 12321 (2011).

8. S. Hore, C. Vetter, R. Kern, H. Smit, and A. Hinsch, "Influence of scattering layers on efficiency of dye-sensitized solar cells," *Sol. Energy Mater. Sol. Cells* **90,** 1176 (2006).

9. Z. Lan, J. Wu, J. Lin, and M. Huang, "A facile way to fabricate highly efficient photoelectrodes with chemical sintered scattering layers for dye-sensitized solar cells," *J. Mater. Chem.* **21,** 15552 (2011).

10. J. K. Lee, B. H. Jeong, S. I. Jang, Y. G. Kim, Y. W. Jang, S. B. Lee, and M. R. Kim, "Preparations of TiO$_2$ pastes and its application to light-scattering layer for dye-sensitized solar cells," *J. Ind. Eng. Chem* **15,** 724 (2009).

11. S. Ameen, M. S. Akhtar, H. K. Seo, Y. S. Kim, and H. S. Shin, "Influence of Sn doping on ZnO nanostructures from nanoparticles to spindle shape and their photoelectrochemical properties for dye sensitized solar cells," *Chem. Eng. J.* **187,** 351 (2012).

12. Q. Zhang, C. S. Dandeneau, S. Candelaria, D. Liu, B. B. Garcia, X. Zhou, Y. H. Jeong, and G. Cao, "Effects of lithium ions on dye-sensitized ZnO aggregate solar cells," *Chem. Mater.* **22,** 2427 (2010).

13. Y. Z. Zheng, X. Tao, Q. Hou, D. T. Wang, W. L. Zhou, and J. F. Chen, "Iodine-doped ZnO nanocrystalline aggregates for improved dye-sensitized solar cells," *Chem. Mater.* **23,** 3 (2011).

14. R. Tao, T. Tomita, R. A. Wong, and K. Waki, "Electrochemical and structural analysis

of Al-doped ZnO nanorod arrays in dye-sensitized solar cells," *J. Power Sources* **214,** 159 (2012).

15. T. Minami, H. Nanto, and S. Takata, "HIGH CONDUCTIVE AND TRANSPARENT ALUMINUM DOPED ZINC OXIDE THIN FILMS PREPARED BY rf MAGNETRON SPUTTERING," *Jpn. J. Apl. Phys.,Part 2* **23,** 280 (1984).

16. S. Yun, J. Lee, J. Chung, and S. Lim, "Improvement of ZnO nanorod-based dye-sensitized solar cell efficiency by Al-doping," *J. Phys. Chem. Solids* **71,** 1724 (2010).

17. S. Yun, and S. Lim, "Improved conversion efficiency in dye-sensitized solar cells based on electrospun Al-doped ZnO nanofiber electrodes prepared by seed layer treatment," *J. Solid State Chem.* **184,** 273 (2011).

18. T. Moon, S. T. Hwang, D. R. Jung, D. Son, C. Kim, J. Kim, M. Kang, and B. Park, "Hydroxyl-quenching effects on the photoluminescence properties of SnO_2:Eu^{3+} nanoparticles," *J. Phys. Chem. C* **111,** 4164 (2007).

19. G. K. Williamson and W. H. Hall, "X-ray line broadening from filed aluminium and wolfram,"*Acta Metall.* **1,** 22 (1953).

20. P. Sagar, M. Kumar, and R. M. Mehra, "Electrical and optical properties of sol-gel derived ZnO:Al thin films," *Mater. Sci.-Poland* **23,** 685 (2005).

21. P. Sagar, M. Kumar, and R. M. Mehra, "Influence of hydrogen incorporation in sol-gel derived aluminum doped ZnO thin films," *Thin Solid Films* **489,** 94 (2005).

22. A. Hagfeldt, G. Boschloo, L. Sun, L. Kloo, and H. Pettersson, "Dye-sensitized solar cells," *Chem. Rev.* **110,** 6595 (2010).

23. J. Jiu, S. Isoda, M. Adachi, and F. Wang, "Preparation of TiO_2 nanocrystalline with 3-

5 nm and application for dye-sensitized solar cell," *J. Photoch. Photobio. A* **189,** 314 (2007).

24. H. W. Lee, S. P. Lau, Y. G. Wang, K. Y. Tse, H. H. Hng, and B. K. Tay, "Structural, electrical and optical properties of Al-doped ZnO thin films prepared by filtered cathodic vacuum arc technique," *J. Cryst. Growth* **268,** 596 (2004).

25. D. V. Lang, and L. C. Kimerling, "Observation of recombination-enhanced defect reactions in semiconductors," *Phys. Rev. Lett.* **33,** 489 (1974).

국문 초록

Zn(S,O) 버퍼층의 밴드갭 (bandgap)과 조성의 변화에 후열처리 과정이 미치는 영향을 살펴보았다. Zn(S,O) 박막의 밴드갭은 후열처리 전 3.59 eV 였지만 500℃ 후열처리에 의해 2.97 eV 까지 감소하였다. 또한 EDX 분석을 통해 얻은 S/Zn 조성비는 열처리 전 0.60 에서 500℃ 열처리 후 0.47 까지 감소하였다. 이는 공기 중에서 진행된 후열처리 과정에서 박막내의 S 가 산소와 결합하여 SO_2 로 산화된 후 승화했기 때문이라고 생각된다. 화학적 용액 성장법을 이용해 FTO 위에 증착된 Zn(S,O) 박막은 염료 감응형 태양전지의 short-circuit current 를 감소시켰다. 이는 증착된 박막의 두께가 너무 두꺼워 광전극의 전자가 FTO 로 이동하기 어려워졌기 때문이라 여겨진다.

가수분해를 통해 Al 도핑 된 복잡 분산 nanoporous ZnO aggregates 를 합성하였다. Al 도펀트 (dopant)는 염료 감응형 태양전지의 short-circuit current 와 open-circuit voltage 를 모두 감소시켰다. XRD 분석결과 Al 의 도핑양이 증가 할수록 ZnO 의 결정립 크기와 로컬 스트레인 (local strain)은 증가하였다. 또한 aggregate 를 이루는 nanoparticle 이 nanorod 로 변한 것을 SEM 을 통해 확인하였다. 이러한 모양변화는 염료가 붙을 수 있는 표면적을 감소시키게 되고, 이 때문에 전지의 효율이 감소하였다고 생각된다.

주요어: CIGS 태양전지, Zn(S,O) 버퍼층, 염료 감응형 태양전지,
ZnO 전지, Al 도핑 ZnO.